



AFRL-AFOSR-VA-TR-2016-0247

Evolution of Zinc Oxide Nanostructures from Non-Equilibrium Deposition Conditions

**XUDONG WANG
UNIVERSITY OF WISCONSIN SYSTEM
750 UNIVERSITY AVE
MADISON, WI 53706-1411**

**07/11/2016
Final Report**

<p>DISTRIBUTION A: Distribution approved for public release.</p>

Air Force Research Laboratory
AF Office Of Scientific Research (AFOSR)/RTB1

Arlington, Virginia 22203
Air Force Materiel Command

DISTRIBUTION A: Distribution approved for public release.

REPORT DOCUMENTATION PAGE					Form Approved OMB No. 0704-0188	
<p>The public reporting burden for this collection of information is estimated to average 1 hour per response, including the time for reviewing instructions, searching existing data sources, gathering and maintaining the data needed, and completing and reviewing the collection of information. Send comments regarding this burden estimate or any other aspect of this collection of information, including suggestions for reducing the burden, to the Department of Defense, Executive Service Directorate (0704-0188). Respondents should be aware that notwithstanding any other provision of law, no person shall be subject to any penalty for failing to comply with a collection of information if it does not display a currently valid OMB control number.</p> <p>PLEASE DO NOT RETURN YOUR FORM TO THE ABOVE ORGANIZATION.</p>						
1. REPORT DATE (DD-MM-YYYY) 16-06-2016		2. REPORT TYPE Final report			3. DATES COVERED (From - To) 27-Mar-2013 to 31-Mar-2016	
4. TITLE AND SUBTITLE Evolution of Zinc Oxide Nanostructures from Non-Equilibrium Deposition Conditions				5a. CONTRACT NUMBER FA9550-13-1-0168		
				5b. GRANT NUMBER		
				5c. PROGRAM ELEMENT NUMBER		
6. AUTHOR(S) Wang, Xudong				5d. PROJECT NUMBER		
				5e. TASK NUMBER		
				5f. WORK UNIT NUMBER		
7. PERFORMING ORGANIZATION NAME(S) AND ADDRESS(ES) BOARD OF REGENTS OF THE UNIVERSITY OF WISCONSIN SYSTEM RESEARCH & SPONSORED PROGRAMS 21 N PARK ST STE 6401 MADISON WI 53715-1218					8. PERFORMING ORGANIZATION REPORT NUMBER 144-PRJ69WY	
9. SPONSORING/MONITORING AGENCY NAME(S) AND ADDRESS(ES) Air Force Office of Scientific Research 875 North Randolph Street Suite 325, Room 3112 Arlington VA, 22203					10. SPONSOR/MONITOR'S ACRONYM(S) ONRRO	
					11. SPONSOR/MONITOR'S REPORT NUMBER(S)	
12. DISTRIBUTION/AVAILABILITY STATEMENT Distribution A - Approved for public release						
13. SUPPLEMENTARY NOTES N/A						
14. ABSTRACT This project focuses on to quantitatively understand the time-dependent evolution of Zinc Oxide (ZnO) nanostructures driven by non-equilibrium deposition conditions, and thereby establish an experimentally grounded foundation for designing nanostructures and/or functionalities via kinetic control. Through vapor-solid deposition under dynamically controlled conditions, we observed three unique 1D and 2D nanocrystal growth behavior, which revealed a series of unique growth kinetics at the nanoscale under conditions far away from equilibrium. First, the wedding cake growth mechanism in the formation of 1D and 2D ZnO nanostructures was observed, which was controlled by the Ehrlich-Schwoebel (ES) barrier as a function of the supersaturation. Furthermore, an inverted wedding cake growth phenomenon was observed in the formation of a unique basin-shaped 2D nanostructure. The morphology and temperature relation revealed the ES barrier of ZnO to be 0.88 eV. A unique high-energy facet evolution phenomenon at the NW tip was further observed at different deposition supersaturation within a narrow vapor deposition window. This project substantially enriches our understanding on the fundamental kinetics of nanostructured crystal growth.						
15. SUBJECT TERMS Non-equilibrium deposition; Supersaturation; Ehrlich-Schwoebel barrier; Wedding cake growth; Crystal facet evolution						
16. SECURITY CLASSIFICATION OF:			17. LIMITATION OF ABSTRACT	18. NUMBER OF PAGES	19a. NAME OF RESPONSIBLE PERSON	
a. REPORT	b. ABSTRACT	c. THIS PAGE			Xudong Wang	
U	U	U	UU	19	19b. TELEPHONE NUMBER (Include area code) 608-890-2667	

INSTRUCTIONS FOR COMPLETING SF 298

1. REPORT DATE. Full publication date, including day, month, if available. Must cite at least the year and be Year 2000 compliant, e.g. 30-06-1998; xx-06-1998; xx-xx-1998.

2. REPORT TYPE. State the type of report, such as final, technical, interim, memorandum, master's thesis, progress, quarterly, research, special, group study, etc.

3. DATES COVERED. Indicate the time during which the work was performed and the report was written, e.g., Jun 1997 - Jun 1998; 1-10 Jun 1996; May - Nov 1998; Nov 1998.

4. TITLE. Enter title and subtitle with volume number and part number, if applicable. On classified documents, enter the title classification in parentheses.

5a. CONTRACT NUMBER. Enter all contract numbers as they appear in the report, e.g. F33615-86-C-5169.

5b. GRANT NUMBER. Enter all grant numbers as they appear in the report, e.g. AFOSR-82-1234.

5c. PROGRAM ELEMENT NUMBER. Enter all program element numbers as they appear in the report, e.g. 61101A.

5d. PROJECT NUMBER. Enter all project numbers as they appear in the report, e.g. 1F665702D1257; ILIR.

5e. TASK NUMBER. Enter all task numbers as they appear in the report, e.g. 05; RF0330201; T4112.

5f. WORK UNIT NUMBER. Enter all work unit numbers as they appear in the report, e.g. 001; AFAPL30480105.

6. AUTHOR(S). Enter name(s) of person(s) responsible for writing the report, performing the research, or credited with the content of the report. The form of entry is the last name, first name, middle initial, and additional qualifiers separated by commas, e.g. Smith, Richard, J, Jr.

7. PERFORMING ORGANIZATION NAME(S) AND ADDRESS(ES). Self-explanatory.

8. PERFORMING ORGANIZATION REPORT NUMBER.

Enter all unique alphanumeric report numbers assigned by the performing organization, e.g. BRL-1234; AFWL-TR-85-4017-Vol-21-PT-2.

9. SPONSORING/MONITORING AGENCY NAME(S) AND ADDRESS(ES). Enter the name and address of the organization(s) financially responsible for and monitoring the work.

10. SPONSOR/MONITOR'S ACRONYM(S). Enter, if available, e.g. BRL, ARDEC, NADC.

11. SPONSOR/MONITOR'S REPORT NUMBER(S). Enter report number as assigned by the sponsoring/monitoring agency, if available, e.g. BRL-TR-829; -215.

12. DISTRIBUTION/AVAILABILITY STATEMENT. Use agency-mandated availability statements to indicate the public availability or distribution limitations of the report. If additional limitations/ restrictions or special markings are indicated, follow agency authorization procedures, e.g. RD/FRD, PROPIN, ITAR, etc. Include copyright information.

13. SUPPLEMENTARY NOTES. Enter information not included elsewhere such as: prepared in cooperation with; translation of; report supersedes; old edition number, etc.

14. ABSTRACT. A brief (approximately 200 words) factual summary of the most significant information.

15. SUBJECT TERMS. Key words or phrases identifying major concepts in the report.

16. SECURITY CLASSIFICATION. Enter security classification in accordance with security classification regulations, e.g. U, C, S, etc. If this form contains classified information, stamp classification level on the top and bottom of this page.

17. LIMITATION OF ABSTRACT. This block must be completed to assign a distribution limitation to the abstract. Enter UU (Unclassified Unlimited) or SAR (Same as Report). An entry in this block is necessary if the abstract is to be limited.

Evolution of Zinc Oxide Nanostructures from Non-Equilibrium Deposition Conditions

PI: Xudong Wang, Materials Science and Engineering, University of Wisconsin-Madison

Introduction

This project focuses on to quantitatively understand the time-dependent evolution of Zinc Oxide (ZnO) nanostructures driven by non-equilibrium deposition conditions, and thereby establish an experimentally grounded foundation for designing nanostructures and/or functionalities via kinetic control. Morphology is one essential element that gives rise to extraordinary physical, chemical, and mechanical properties in nanomaterials. Precise morphology control of nanomaterials is a notorious task, which heavily relies on fundamental understanding of the governing atomistic mechanisms and kinetics at the nanoscale. Through vapor-solid deposition under dynamically controlled conditions, we observed three unique 1D and 2D nanocrystal growth behavior, which revealed a series of unique growth kinetics at the nanoscale under conditions far away from equilibrium. First, the wedding cake growth mechanism in the formation of 1D and 2D ZnO nanostructures was observed within a narrow growth window. An interesting 1D to 2D morphology transition was also found during the wedding cake growth, when the adatoms overcome the Ehrlich-Schwoebel (ES) barrier along the edge of the top crystal facet triggered by lowering the supersaturation. Furthermore, an inverted wedding cake growth phenomenon was observed in 2D nanostructure evolution. The atomic steps were nucleated along the edge and propagated toward the center forming a unique basin-shaped crown on the tip of each nanowire. The morphology and temperature relation revealed the ES barrier of ZnO to be 0.88 eV. Based on the layer-by-layer growth model, a unique high-energy facet evolution phenomenon at the NW tip was observed at different deposition supersaturation within a narrow vapor deposition window. The facets evolution and exposure of high-energy facets were attributed to the fluctuation of the energy barriers for the formation of different crystal facets during the growth of NW tip. This project substantially enriches our understanding on the fundamental kinetics of nanostructured crystal growth and provides a transformative strategy to achieve rational design and control of nanoscale geometry.

1. Observation of wedding cake growth mechanism

We reported an observation of the wedding cake growth mechanism in the formation of 1D and 2D ZnO nanostructures. The wedding cake growth model yields a very similar terraced surface as that generated by a screw dislocation but does not possess a dislocation core and spiral pattern. An interesting 1D to 2D morphology transition was also found during the wedding cake growth, when the adatoms overcome the Ehrlich-Schwoebel (ES) barrier along the edge of the top crystal facet, triggered by lowering the supersaturation.

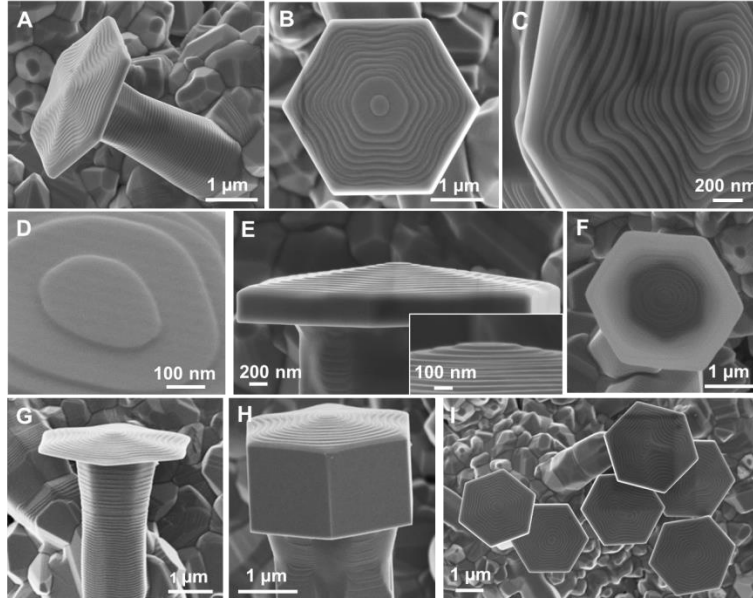


Figure 1. Morphology of microplate-capped micropillars. **A.** An individual microplate-capped micropillar clearly shows a thread-like feature on both plate and pillar surfaces. **B.** Top view of a microplate exhibiting a hexagonal outline with multiple concentric terrace circles. **C.** Tilted and enlarged view of a microplate showing the intermediate sub-terraces extruding along the six equivalent corner directions. **D.** A flat and smooth central terrace surface without any observable screw dislocation steps. **E.** Side view of a microplate showing the terraced structure descending from the center of the plate. Inset shows the flat top terrace. **F.** An image of a very thin microplate revealing orientation of the microplate and micropillar is differentiated by 30°. **G.** and **H.** Examples of plate-capped micropillars with small (**G**) and large (**H**) plate thicknesses. **I.** Irregular terrace patterns due to the shadowing effect at high plate density region.

The unique ZnO microstructure was obtained under a dynamic deposition condition, where the growth chamber temperature was rapidly increased from room temperature to 1673 K within 90 min. During the ramp, both the Zn vapor concentration and the ZnO deposition temperature rose continuously. The ZnO microstructure composes a micrometer-sized pillar that was capped with a large hexagonal microplate (Fig. 1A). The pillars were typically several micrometers long with a diameter of ~1 micrometer. The microplates were ~2-3 micrometers in diameter with variable thicknesses. A thread-like feature can be clearly observed both along the side of the pillar and on the plate surface. The top microplate exhibited a sharp hexagonal outline with multiple concentric terraces (Fig. 1B). These terraces, however, did not exhibit a sharp hexagonal outline as the microplate showed, whereas extrusions together with intermediate sub-terraces (indication of rapid growth front) can be observed along the six equivalent corner directions (Fig. 1C). Although this surface feature is very much similar to a screw dislocation growth pattern, a spiral center, which is the characteristic feature of a screw dislocation-driven growth, could not be observed. All the plates exhibited a flat and smooth central terrace surface (Fig. 1D). This phenomenon fits well to the wedding cake growth model, where new atomic layers nucleate on the current top layer giving rise to a wedding cake like structure. A side view of the plate clearly displays the step-wise terrace configuration (Fig. 1E), indicating the terraces were evolved initially at the center and then spread out to the edge. A zoomed-in image also evidences the flat top terrace without a spiral center (inset of Fig. 1E).

From very thin plates that electrons can penetrate through, the orientation relationship between the plate and pillar can be observed. As shown in Fig. 1F, the darker hexagon at the center of the plate outlines the pillar underneath. The hexagonal capping plate exhibited a 30° rotation in its orientation. Based on the crystallography of wurtzite ZnO, this feature suggests that the six equivalent side facets of the pillar and the plate are either one of the two low-energy surfaces of $\{01\bar{1}0\}$ and $\{11\bar{2}0\}$, respectively. The thickness of the plates exhibited a large variation ranging from 50 nm to $\sim 1\ \mu\text{m}$ (Fig. 1G, H). Regardless of the thickness, all the plates had a very uniform width along their entire thickness with a clear convex terraced top surface. While most plates exhibited a six-fold symmetric terrace pattern, irregular terrace patterns could be observed at high density region (Fig. 1I). Shadowing effect or competition of precursor might be responsible for the asymmetric growth behavior.

The crystal structure of ZnO plate-caped micropillars was characterized by Cs-corrected scanning transmission electron microscopy (STEM). Selective area electron diffraction (SAED) pattern taken from the cross-sectional structure revealed that the entire structure was a single crystal and grew along the $\langle 0001 \rangle$ direction. The height of each terrace was in a range of 5~20 nm. The terrace edge was not perpendicular to the plate surface and all of them showed a slope of $\sim 153^\circ$. High resolution STEM (HR-STEM) images taken at the plate-pillar joint region showed a coherent crystal lattice and no grain boundary or other dislocations could be found. Particularly, no indication of the existent of a screw dislocation core was discovered along the center position where the top terraces nucleated. The terrace edge was found composed of multiple small steps without any dislocations, consistent with SEM observations. The HRTEM observations further evidence that the wedding cake growth model governed the evolution of ZnO crystals.

Supported by microscopy observations, the wedding cake growth model is used to analyze the evolution of the 2D microplates. In a wedding cake growth, formation of surface terraces relies on nucleation of new atomic layers on the top surface due to the accumulation of concentrated adatoms confined by the energy barrier at step edges. This yields the representative morphology of concentric circular mounds without a spiral feature. The wedding cake growth behavior was mostly observed in the low temperature epitaxial growth of metal surfaces. However, in our hybrid structure, evolution of suspended 2D plates requires the lateral growth to exceed the supporting pillar's top surface. Therefore, the adatoms need to overcome the ES barrier which prevents adatoms from diffusing down at the terrace edge and then incorporated at the corner along the vertical facets. Lattice kinetic Monte Carlo (LKMC) method was used to simulate the morphology evolution when the ES barrier becomes tangible. This simulation verifies that the ES barrier triggers the formation of the suspended plate morphology through decreasing the supersaturation.

To better understand the wedding cake growth mechanism in nanostructure evolution, numeric calculations were implemented to analyze the growth rates along different directions in comparison to the screw dislocation-driven growth mechanism. In a wedding cake growth, the lateral growth rate v_l is a measure of how fast adatoms attach to the ledge front, which is same as that in a screw dislocation growth. Quantitatively, v_l can be presented following the Burton-Cabrera-Frank (BCF) theory:

$$v_l = \frac{2\lambda_s \nu \exp(-\frac{\varphi_{1/2}}{kT})}{1 + \frac{\delta}{a} \exp(\frac{2\Delta U - E_{des}}{2kT})} \sigma \quad (1)$$

where a is the distance between adsorption sites, ν is the vibration frequency, $\varphi_{1/2}$ is the work to detach an atom from half-crystal position to the vapor, k is the Boltzmann constant, T is temperature, σ is the supersaturation, λ_s is the mean free path of an adatom, δ is average spacing of the kink sites, ΔU is the kinetic barrier for the incorporation of the building units into the half crystal, and E_{des} is the desorption energy from the surface to the vapor.

As for the vertical growth rate v_a , in the wedding cake model, it is directly related to the nucleation rate of new layers, which occurs only when the top layer reaches a critical size. Therefore, the vertical growth rate can be formulated as:

$$v_{a,w} = \frac{h}{R_c} v_l \quad (2)$$

where R_c is the critical size of the top layer and h is the height of the newly formed terrace. On the other hand, the vertical growth rate of the screw dislocation model follows the BCF theory:

$$v_{a,s} = a \nu \exp(-\frac{\varphi_{1/2}}{kT}) \frac{\sigma^2}{\sigma_c} \tanh \frac{\sigma_c}{\sigma} \quad (3)$$

where σ_c is characteristic supersaturation. Since there is no nucleation involved in the screw dislocation growth, wedding cake model usually exhibits a slower vertical growth rate.

One direct result of the different axial and lateral growth rates is the number of terraces on the plate surface. Shown in Figure 2A, within the deposition area (~ 2 mm in length) where terraced plates were received, the number of terraces decreased as the sampling point moved along the gas flow (downstream) direction, whereas no obvious size variation could be identified.

Then we converted the number of terraces into growth rate ratio. By rearranging the expression of lateral growth rate (Eq. 1), the relation is displayed as below:

$$v_l = \frac{2\sigma \nu \exp(-\frac{\varphi_{1/2}}{kT})}{1 + \frac{\delta}{a} \exp(\frac{2\Delta U - E_{des}}{2kT})} \lambda_s \quad (4)$$

For any given plate structure, we assume σ and T are constant, and thus the lateral growth rate is linearly related to λ_s . Therefore, when λ_s decreases, v_l decreases.

To determine axial to lateral growth rate ratio, we assume the time spent by the first terrace (the base terrace) to grow from the plate center to the plate edge (t_l) equals to the time to evolve the rest terraces (t_a). The base terrace expands with a velocity of $v_{l,1}$ and then decreases to $v_{l,2}$ when approaching the edge due to the decrease of effective adatom collection area ($t_l = t_{l,1} + t_{l,2}$). The height from the base terrace to the plate top is nh , where n is the number of the terraces and h is the height of one step. Thus,

$$t_a = \frac{nh}{v_a} = \frac{R - \lambda_s}{v_{l,1}} + t_{l,2} \quad (5)$$

where R is the plate radius. From the equation of the lateral growth rate (Eq. 4), we can get the expression for $v_{l,1}$:

$$v_{l,1} = A\lambda_s \quad (6)$$

where the coefficient A is a constant by assuming that σ and T are constant during the growth of a specific microplate:

$$A = \frac{2\sigma\nu \exp(-\frac{\phi_{l/2}}{kT})}{1 + \frac{\delta}{a} \exp(\frac{2\Delta U - E_{des}}{2kT})}$$

As for $v_{l,2}$:

$$v_{l,2} = A(\lambda_s - x) \quad (7)$$

where x is the distance the terrace grows with the velocity $v_{l,2}$. $(\lambda_s - x)$ represents the distance from the terrace edge to the plate edge. This equation expresses the instantaneous velocity at the point $(\lambda_s - x)$ because $v_{l,2}$ varies with the effective collection area. $v_{l,2}$ can be expressed in terms of $v_{l,1}$ as:

$$v_{l,2} = \frac{\lambda_s - x}{\lambda_s} v_{l,1} \quad (8)$$

Then $t_{l,2}$ can be obtained by integrating from $x = 0$ to $x = (\lambda_s - d)$:

$$t_{l,2} = \int_0^{\lambda_s - d} \frac{dx}{v_{l,2}} = \int_0^{\lambda_s - d} \frac{dx}{\frac{\lambda_s - x}{\lambda_s} v_{l,1}} = \frac{\lambda_s}{v_{l,1}} \ln \frac{\lambda_s}{d} \quad (9)$$

Insert Eq. 9 into Eq. 5, we get:

$$\frac{nh}{v_a} = \frac{R - \lambda_s}{v_{l,1}} + \frac{\lambda_s}{v_{l,1}} \ln \frac{\lambda_s}{d} \quad (10)$$

Rearrange Eq. 10 to get the growth rate ratio:

$$\frac{v_a}{v_{l,1}} = \frac{nh}{(R - \lambda_s) + \lambda_s \ln \frac{\lambda_s}{d}} \quad (11)$$

The values of n , h and d can be obtained by measurement, therefore the number of terraces n is converted to the growth rate ratio $v_a/v_{l,1}$.

Next, the position was converted to the supersaturation. The local vapor pressure is obtained by subtracting the amount consumed by deposition from the initial amount yielded by the

precursor source. According to the previous results, the deposition of ZnO from the vapor phase underwent two steps, zinc condensation and zinc oxidation. At high temperature (>700 K), the condensation of zinc is the rate-limiting step. Therefore, we use the condensation rate of zinc as the deposition rate. The condensation rate is determined by the sticking coefficient (S) and the incident molecular flux (F) via $R_{con} = F \times S$, where S is estimated to be 0.1 and F is obtained from the Hertz-Knudsen equation:

$$F = \frac{P - P_e}{(2\pi mkT)^{1/2}} \quad (12)$$

where P is the partial pressure of zinc, P_e is the equilibrium partial pressure of zinc at the deposition location, m is the mass of zinc atom, and T is the local temperature (1670 K in this case). Because there was no deposition prior zinc vapor reached the growth region of plate-caped micropillar structure, we can use the total amount yielded by the precursor as the initial partial pressure of zinc to calculate the condensation rate of zinc for the formation of plate-caped micropillar structure.

The unit for zinc condensation rate R_{con} is $\text{mol}/(\text{m}^2 \cdot \text{s})$. It gives the deposition amount per second per square meter. For an infinitesimal distance dx , the deposition time is dx/r , where r is the flow rate of the carrier gas. The flow rate was obtained from the flowmeter of the CVD system, and then converted to the flow rate in the growth chamber considering the pressure and temperature in the chamber by a rough estimation using $PV = nRT$. The deposition area is the internal surface of the tubular chamber, $\pi \cdot D \cdot dx$, where D is the internal diameter of the furnace tube. The deposition volume is $\pi(D/2)^2 dx$. Thus, the amount of deposition at this infinitesimal area per unit volume (*i.e.* the vapor concentration reduction) is

$$\Delta c = \frac{\pi \cdot D \cdot dx \cdot \frac{dx}{r} \cdot R_{con}}{\pi \cdot \left(\frac{D}{2}\right)^2 \cdot dx} \quad (13)$$

Eq. 13 is rearranged and simplified as:

$$\Delta c = \frac{4R_{con}}{D \cdot r} \cdot x \quad (14)$$

where x is the distance from the deposition starting point to the point of interest. The deposition starting point can be measured from the experiment.

Using $P = cRT$ to convert the concentration to pressure, we can combine Eq. 14 and $\sigma = P/P_e - 1$ to get:

$$\sigma = \frac{(c_0 - \frac{4R_{con}}{D \cdot r} \cdot x)RT}{P_e} - 1 \quad (15)$$

Arranging Eq. 15, we have:

$$\sigma = \frac{c_0 RT - P_e}{P_e} - \frac{4R_{con} \cdot RT}{P_e \cdot D \cdot r} \cdot x \quad (16)$$

Through this equation, the position of the microplate can be converted to the local supersaturation.

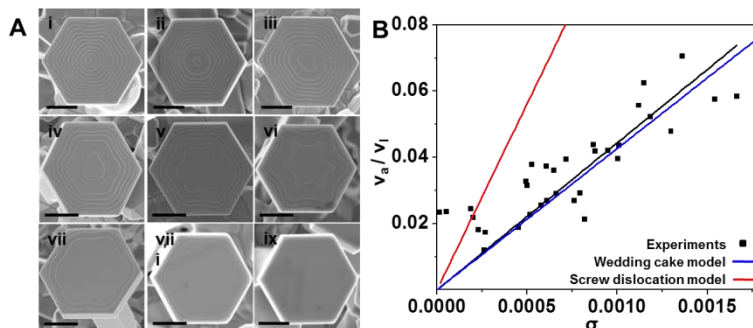


Figure 2. Wedding cake growth model. **A.** Microplates with various numbers of terraces. The number of terraces decreased as the sampling point moved along the gas flow (downstream) direction. i–ix are microplate samples collected at position 16.8479 cm, 16.8664 cm, 16.8669 cm, 16.9033 cm, 16.9189 cm, 16.9256 cm, 16.9459 cm, 16.9741 cm, and 17.0129 cm from the center point, respectively. All the scale bars are 1 μ m. **B.** Plots of the axial to lateral growth rate ratio as a function of supersaturation. Black dots are measured data. Black line is the fitted curve based on the measured data, where a linear relationship can be determined. Blue line is derived from wedding cake growth model. Red line calculated is from screw dislocation growth model for comparison.

This relation shows that the v_a/v_l ratio increases with supersaturation, suggesting a trend that the number of terrace increases with supersaturation in Figure 2B. The significantly closer match of the wedding cake model over screw dislocation model further evidences the governing role of the wedding cake mechanism in the evolution of ZnO microplate structure.

In order to reveal the σ -related evolution of wedding cake tip morphology in a more general NW growth scenario, the deposition condition was adjusted to reach desired σ for NW formation. Under this condition, ZnO NWs were formed with uniform size and geometry, where each NW exhibited a terraced tip feature. Just like the microplates, the central terrace exhibited a flat surface and no hint of the existence of any screw dislocation could be observed by both SEM and TEM characterizations. All the observations evidenced the wedding cake growth mechanism in the formation of these NWs. Furthermore, the tip terrace feature exhibited the same relation with the deposition temperature as that observed from microplates. When the deposition temperature decreases, the number of terrace at the NW tip decreases and eventually the flat tip morphology was obtained. After a relative large temperature range, the suspended microplate morphology appeared, suggesting the deposition condition reached the critical low σ region. Similar change could also be observed by increasing the oxygen partial pressure. Qualitatively, high oxygen content in the reaction chamber hinders the decomposition of ZnO precursors and thus lowers σ . Therefore, as the oxygen partial pressure increased, the NW tip exhibited the similar change from a large number terraced surface to a flat tip.

2. Observation of inverted wedding cake growth mechanism

Another wedding cake-related growth phenomenon was observed, which was similar to the step edge growth in VSS processes. A series of single crystal hexagonal branch-crowned ZnO

NW structure was obtained by dynamically changing the deposition temperature during the growth. The top structure was found to be a basin-like concave crown with six equivalent extended branches. An inverted wedding cake growth model involving the Ehrlich-Schwoebel (ES) barrier and step propagation along the top surface edge was developed to explain the growth mechanism. By changing the oxygen partial pressure and deposition temperature, the ES barrier of ZnO was quantified.

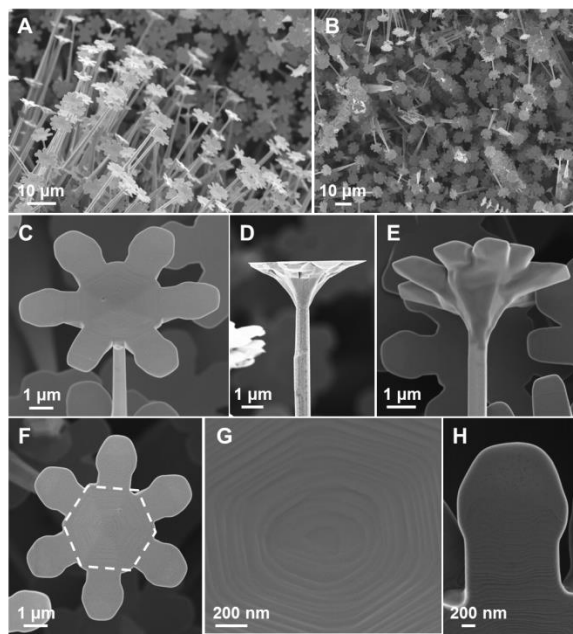


Figure 3. Morphologies of crown-capped NW structures. **A.** Large scale side view and **B.** top view of the crown-capped NW arrays. **C.** A tilted top view, **D.** a side view, and **E.** a tilted bottom view of an individual six-branched crown cap structure. **F.** A top view of the crown surface showing the hexagonal center pattern. **G.** Enlarged image on the crown center, showing the hexagonal concentric steps. **H.** Enlarged image on one branch, showing a large flat surface area around the tip of the branch and the steps became more regularly spaced near the center region.

Dynamically controlled VS growth of ZnO nanostructures was carried out under dynamically-tuning deposition conditions. Both the evaporation and deposition temperature was increased during the growth providing a non-steady state growth environment. The rapid change of vapor concentration by the end of growth period yielded a unique morphology-switch growth phenomenon, where all the NWs were capped with a significantly broadened crown, as shown by the side-viewed SEM image in Figure 3A. Different from our previous observations of the hexagon-capped nanopillars, all the top crowns exhibited clear six-fold branches with uniform sizes and distributions (Fig.3B). Figure 3C shows a typical structure of the hybrid morphology. The NW had a diameter of ~ 500 nm and a length of ~ 30 μm or even longer. The crown had a core diameter of ~ 3 μm and six branches, which expanded up to ~ 7 μm wide. Side view in Fig. 3D shows that the crown had a basin-like shape, where the diameter gradual increased from ~ 500 nm at the NW junction to ~ 7 μm at the top. When observed from the bottom as shown in Fig. 3E, the junction between the NW and crown showed a very smooth transition and no discontinuity could be identified.

The top view in Fig. 3F reveals more details about the crown's surface features. The crown center had a hexagonal outline as marked by the white dashed line and six branches grew out from the six edges of the hexagon. The enlarged view of the plate center in Fig. 3G shows the surface was featured by concentric hexagonal circular steps. At the innermost circle, there was a flat surface and no screw dislocation spiral center could be identified. Different from our previous observations, the step height increased from the plate center to plate edge, forming a concave surface instead of the classic mount-shaped feature. Similar step structure could also be observed on the branch surface (Fig. 3H). At the very front branch tip region, a relatively wide flat surface area was commonly observed, which could be more than 1 μm wide. The initial steps exhibited larger step width than the steps in the center region. The front of each step was not straight and does not represent any crystal facets. The flat area also covered a small area along the edge of the branches as marked by dashed lines, indicating edge nucleation and growth was much more favorable than other positions on the plate. These morphological features suggested that new atomic layers would nucleate first at the edge, propagate inward, and slow down when approaching the previous step due to the limited quantity of adatoms on the surface.

The crystal structure of the crown and junction region was characterized by transmission electron microscopy (TEM). HRTEM images were taken from the joint part between the crown and the NW. It showed that the lattice was continuous at the connection and no dislocation core could be observed. The SAED pattern also confirmed the single crystal feature of the entire hybrid structure.

In this model, the layer-by-layer growth was initiated at the plate edge instead of nucleating at the center as regular wedding cake growth. The newly formed atomic layers then propagated toward the plate center as adatoms adsorbed and diffused toward the nucleation sites, which thus formed a circular step along the plate edge. The expansion of the top surface is a result of the diffusion down of the adatoms by overcoming the ES barrier. Since the ES barrier prevents the adatoms from overcoming the crystal ledge, it helps increase the concentration of surface adatoms and thus facilitates the nucleation of new atomic layers. According to our previous results, as the supersaturation (σ) decreases, the chance for adatoms to overcome the ES barrier rises, while the concentration of surface adatoms drops. At a certain small σ , the top surface would become no longer a favorable place for nucleation of new atomic layers due to the reduced adatom concentration. Instead, the adatom concentration rises at the crystal edge which becomes a new nucleation site. Therefore, new atomic layers start to form along the edge of the top surface while it becomes wider as the adatoms continuously attach to the edge. In typical mount morphology, the top layer has the largest flat area due to the slower nucleation rate compared to the ledge expansion rate (nucleation-limited region). Similarly, in the inverted wedding cake growth, the top most layer, which is the surface along the edges of the branches, also exhibited the largest flat surface area (Fig. 2H). As the steps approaching the center area, the space between them became much smaller. This is consistent with the fact that the step growth slows down when it approaches the growth front of its previous one due to the decrease of the effective adatom diffusion area, suggesting a mass-transport limited growth region. The large step height also suggested that the step bunching effect was a common growth feature in ZnO layer-by-layer growth due to the high possibility for adatoms to overcome the ES barrier during steps propagation.

In order to further understand how the inverted wedding cake growth is related to conventional wedding cake growth of NWs, a series of syntheses with different oxygen partial

pressures were conducted. The oxygen partial pressures and the temperature zones would modify both the condensation and oxidation rates of zinc, and thus influence the growth kinetics. In the highest temperature region, the nanostructures appeared in the form of NWs with a clear mount-shaped top surface. In the medium temperature zone, a hexagonal plate appeared at the top of each NW and a concave center started to develop. As temperature further reduced, the top plate clearly showed the basin shape and six equivalent branches evolved and elongated from the plate edge. The size of the plates also increased when lowering the deposition temperature. When applying different oxygen partial pressures, the same trend was observed. NW morphology was obtained at the lowest oxygen partial pressure. Increasing the oxygen partial pressure led the top morphology evolution from mount-shape hexagonal plates to basin-shaped branched structures.

The unique morphology switching phenomenon could be understood by the dynamic deposition condition change during the growth processes. At the beginning, the deposition temperature was relatively low, which keeps the equilibrium partial pressure (P_e) at a relatively low level. Since the precursor vapor concentration (P) remained at a relatively high level, σ at any deposition temperature was large. This condition favored NWs growth through the layer-by-layer wedding cake model along the [0001] direction. At this stage, the adatoms were confined at the top (0001) surface and the diffusing down was significantly restricted by the ES barrier. As the deposition temperature rises, P_e increased rapidly leading to a quick drop of σ . The reduction of σ was the most prominent at the highest deposition region, leaving insufficient time for crown formation. Thus, NWs with a mount-shaped tip was obtained as the final product. Meanwhile, relatively small σ was still remained at lower deposition temperature zones. Such a condition favored the diffusion down of the adatoms from the top surface by overcoming the ES barrier and nucleated an additional layer circling around the tip of the NW broadening the top layer. As the diffusion down proceeded, the top surface became undersaturated for nucleating new atomic layers and the growth was completely initiated from the edge. Thus, the growth mode switched to the inverted wedding cake growth and the hexagonal crowns were formed. The growth could be terminated at this stage when P_e further increased to diminish σ at the medium deposition temperature zone. However, at the even lower deposition temperature region, σ could be favorable for lateral growth and larger crowns were obtained in that region. The appearance of six branches might be a result of oxygen adsorption that selectively restricted the growth on the flat edge area. High oxygen partial pressure hinders the decomposition of ZnO precursor and thus lowers σ . Hence, the high oxygen partial pressure favors the growth of the crown featured morphologies and also promotes the formation of branched structure.

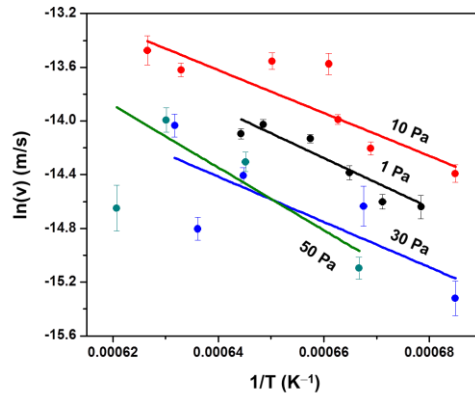


Figure 4. Relationship between the growth rate of microplates and temperature under different oxygen partial pressure, 1 Pa (black dots), 10 Pa (red dots), 30 Pa (blue dots) and 50 Pa (green dots). The correspondingly colored lines are fitted curves which give similar slopes revealing the activation energy for overcoming the ES barrier. Each dot is the average value of ten sets of experimental data from the same temperature region and error bars show standard error.

In general, the plate expansion is a kinetic process, which is determined by the diffusion down rate (α). The relationship between α and the ES barrier (E_{ES}) follows the equation:

$$\alpha = \exp\left(-\frac{E_{ES} - E_{sd}}{kT}\right) \quad (17)$$

where E_{sd} is the surface diffusion barrier, k is the Boltzmann constant, and T is temperature. Therefore, the deposition temperature-related plate morphology can be used to identify the ES barrier for ZnO nanostructure growth. From Eq. 17, the growth rate of the suspended plate due to adatom diffusing down to the edge (v_d) can be derived as a function of T .

$$\ln v_d = \ln \frac{a^4}{\delta \sqrt{2\pi m k}} - \left(\frac{E_{ES} - E_{sd} + \Delta U}{k} + 9087.7 \right) \frac{1}{T} \quad (18)$$

where a is the distance between adsorption sites, ΔU is the kinetic barrier for the incorporation of the building units into the half crystal, δ is average spacing of the kink sites, and m is the mass of zinc. v_d can be determined by comparing the suspended length and the corresponding height of plates, which represents the ratio between vertical growth rate and diffusion down rate. Through this method, v_d was identified from each temperature zone from samples grown under different oxygen partial pressures. The Arrhenius plots of $\ln v_d$ vs. $1/T$ under the four selected oxygen partial pressures showed that the linear fits of the data exhibited very close slopes, from which the ES barrier E_{ES} was found to be $\sim 0.88 \pm 0.33$ eV, in Figure 4. Compared to the reported values in other materials (0.52 eV for Au, 0.40 eV for Cu and 0.12 eV for Al), the value we identified was much higher. This could be the reason that the diffusion down phenomenon was not commonly observed in oxide nanocrystals.

3. Kinetics-Driven Crystal-Facets Evolution at the Tip of Nanowires – A New Implementation of the Ostwald-Lussac Law

Through controlling the growth kinetics, the facets evolution involving the appearance of the high index facets at the nanowire tips was observed. The facets evolution was induced by the change of the relative growth rates of different facets and it followed the Ostwald-Lussac Law. The results provide a platform to understand the nanowire growth mechanism from the vapor phase.

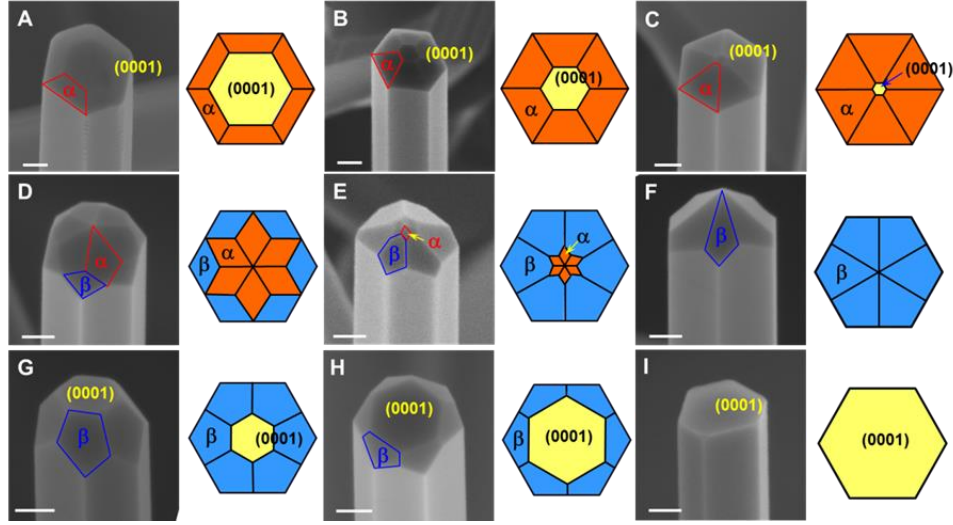


Figure 5. SEM images and corresponding schematic showing facets evolution at NW tips. (A) – (C) NW with the tip enclosed by six α facets and one facet (0001). From (A) to (C), facet (0001) gradually decreased when facets α increased simultaneously. (D) – (F) NW with the tip covered by six α facets and six β facets. From (D) to (F), facets β appeared, expanded and eventually covered the entire tip area at the expenses of facets α . (G) – (I) NW with six β facets and one (0001) facet co-existed tip. From (G) to (I), facets β gradually vanished and facet (0001) appeared again with a 30° rotation relative to the six sidewall of the NW. In the schematic, yellow represents facet (0001), orange is facets α , and blue is facets β . All scale bars are 100 nm.

ZnO NWs were grown through a dynamically controlled vapor-solid deposition. During the NW growth, both the evaporation temperature and the deposition temperature were steadily increased in order to achieve an accelerated dynamic growth environment to make possible the appearance of the thermodynamically unstable morphology growth. Under such a non-steady state deposition condition, randomly-oriented submicron-sized ZnO NWs were grown on the polycrystalline alumina substrate within a broad temperature range from 1300 K to 1673 K. The NWs were typically 20 μm long with a diameter of ~ 300 nm. Most NWs exhibited a clear hexagonal cross section due to the $P6_3mc$ lattice symmetry of the wurtzite crystal structure. Distinguishing from common ZnO NWs that typically have a flat hexagonal (0001) tip facet, the tips of ZnO NWs received from the dynamic deposition condition were mostly enclosed by at least two groups of crystal facets. These tip facets also distributed with a hexagonal symmetry. The NW tip facets evolution were only found at a high deposition temperature region (1665K) and directly related to the deposition location. As shown by the relationship between deposition temperature and location in the deposition chamber in Figure S2, the temperature was almost constant within that region. At other deposition region, the NWs tip was the regular flat (0001) facet. Within this narrow deposition region window (~ 1 cm), different crystal facets evolved and vanished as the deposition location changed slightly.

Representative tip morphology illustrating the tip facets evolution as a function of location and corresponding schematic drawing are presented in Figure 5. At the position closest to the chamber center (17.7 cm from the chamber center, where the precursor source was located), the NW's tip was only partially covered by the hexagonal (0001) facet at the center, with six angled facets (named as α facet) evenly distributed along the six edges between the vertical sidewall

facet and the top (0001) facet, as shown in Figure 5A. As the deposition position moved slightly downstream by ~ 3 mm, the six α facets gradually expanded and eventually occupied the entire tip area (Figure 5A to C). Meanwhile, the (0001) facet shrank into a sharp point at the center of the tip (Figure 5A to C). Subsequently, another group of facets (named as β facet) emerged at the six radial corners of the tips (Figure 5D). The β facets expanded and eventually covered the entire tip area at the expenses of the α facets as the deposition position moved downstream by another ~ 3 mm (Figure 5D to F). At the position slightly farther away from the chamber center, the hexagonal (0001) facet appeared again from the center of the tip. Different from the original (0001) facet obtained from the high-temperature NWs, however, the re-emerged (0001) facet exhibited a 30° rotation relative to the hexagonally-distributed NW sidewalls (Figure 5G). The (0001) facet expanded and eventually took over the entire NW tip again at the deposition position of 18.7 cm away from the chamber center, where the β facets vanished completely (Figure 5H, I). Across this narrow deposition region, the deposition temperature difference was negligible ($< 5^\circ\text{C}$). The vapor pressure of the precursor changed significantly due to the rapid deposition across this region. These suggested that the precursor supersaturation was the dominating factor at this high deposition temperature area. Thus, the facet evolution is primarily correlated to the location-induced supersaturation difference.

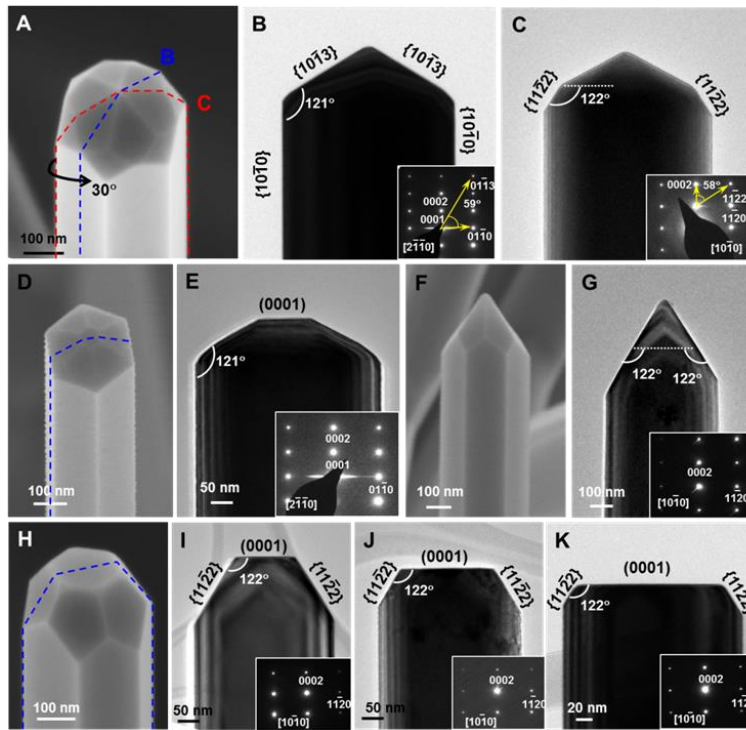


Figure 6. SEM images and TEM projections for facets indexing. (A) NW with facets $\{11\bar{2}2\}$ and facets $\{10\bar{1}3\}$ co-existed tip. TEM projection and selected area electron diffraction (SAED) patterns (inset) along (B) the direction $[2\bar{1}\bar{1}0]$ and (C) the direction $[10\bar{1}0]$. (D) NW with facets $\{10\bar{1}3\}$ and facet (0001) co-existed tip and (E) the corresponding TEM projection. Inset is the SAED pattern along $[2\bar{1}\bar{1}0]$. (F) NW with tip totally solely covered by facets $\{11\bar{2}2\}$ and (G) corresponding TEM projection. Inset is the SAED pattern along $[10\bar{1}0]$. (H) NW with facets $\{11\bar{2}2\}$ and facet (0001) co-existed tip and (I-K) corresponding TEM projection. Insets are the

SAED patterns along $[10\bar{1}0]$ showing the facets $\{11\bar{2}2\}$ and facet (0001) evolution under different supersaturation.

In order to understand the tip facets evolution phenomenon, the involving facets were indexed first. Transmission electron microscopy (TEM) was implemented to characterize selected NW tips from various projection directions. A NW with both the α and β facets was imaged as shown in Figure 6A. TEM image was first recorded along the $[2\bar{1}\bar{1}0]$ projection direction, where only the α facets can be seen (Figure 6B). The projection plane was also outlined by the dashed blue line in Figure 6A. Thus, the angle between the $\{10\bar{1}0\}$ and α facets was directly measured to be 121° from the projected image, which matches well to the selective area electron diffraction (SAED) pattern (inset of Figure 6B). It is noted that in the SAED pattern, presence of the forbidden Bragg spots of the (0001) and (0003) planes was attributed to the secondary Bragg electron diffraction according to the satisfied condition (*e.g.*: $(0\bar{1}11) + (0\bar{1}10) = (0001)$). Therefore, the α facet was indexed to be facets $\{10\bar{1}3\}$, a high index plane. By tilting the same NW by 30° along the NW's axial axis (the $[0001]$ direction), another projection consisting of both the α and β facets were imaged, as shown in Figure 6C. The SAED pattern (the inset of Figure 6C) confirmed that projection was now along the $[10\bar{1}0]$ direction. The geometry of the projected image was outlined by the dashed red line in Figure 6A. At this condition, the β facets were parallel to the electron beam, enabling the measurement of the angle between the β facets and the horizontal plane (known to be the (0001) plane). The angle was measured to be 122° . Therefore, from the corresponding SAED pattern (inset of Figure 6C), the β facet was determined to be $\{11\bar{2}2\}$, another high index plane.

NWs at different evolution stages were collected to further confirm the combination of tip facets. One NW with the $\{10\bar{1}3\}$ facets co-existed with the (0001) facet at the tip was imaged and characterized (Figure 6D). A TEM image was taken from a projection plane of $\{2\bar{1}\bar{1}0\}$ (Figure 6E), as outlined by the dashed blue line in Figure 6D. The orientation was validated by the corresponding SAED pattern (inset of Figure 6E), which was the same as the SAED pattern of the projection in Figure 6B. The angle between the $\{10\bar{1}3\}$ facet and the $\{10\bar{1}0\}$ facets was measured to be 121° , identical to that value measured in Figure 6B, confirming the same facets configuration in this NW tip. Another NW with the tip solely covered by six $\{11\bar{2}2\}$ facets (Figure 6F) was imaged along the $[10\bar{1}0]$ direction (Figure 6G). The angle between the $\{11\bar{2}2\}$ facet and the horizontal plane (dashed line, (0001)) was measured to be 122° , indicating the same facet group as those shown in Figure 6C. Another NW with the combination of $\{11\bar{2}2\}$ and (0001) facets at the tip is shown in Figure 6H. TEM image projected along the $[1\bar{1}00]$ direction is shown in Figure 6I. The angle between the flat tip and the $\{11\bar{2}2\}$ facet was measured to be 122° , identical to the measurement when the (0001) facet was not adjacent (Figure 6C). All these measurements confirmed that there were the same groups of crystal facets during the tip morphology evolution. The TEM image also showed clear thickness fringes around the NW edges. The different fringe patterns from outside to the center directly correlated to the facets organization. Other NWs obtained at slightly farther away from the chamber center that had the same facets combination but increasing (0001) areas are also shown in Figure 6J and 6K. All the SAED patterns and facets angles were identical, confirming no more new facets were evolved when the NW tip was reclaimed by the (0001) facet again.

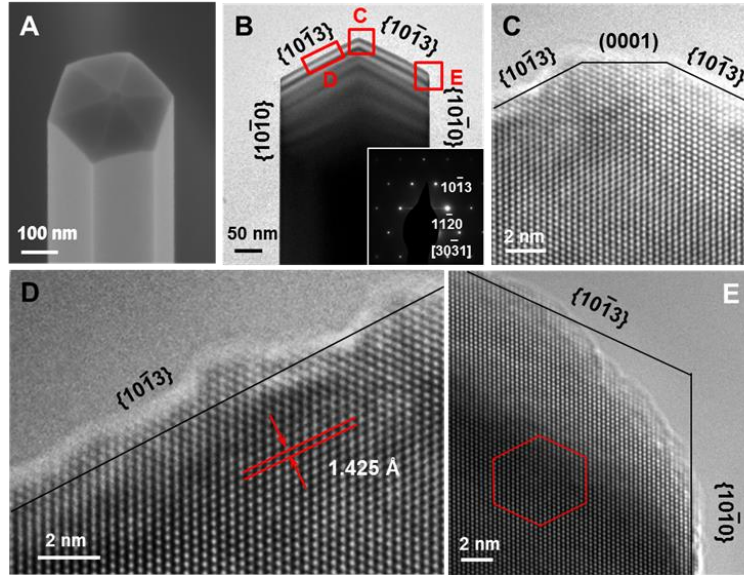


Figure 7. High resolution TEM images on the lattice structure at the NW tip. (A) NW with the tip predominately covered by facets $\{10\bar{1}3\}$ and (B) the corresponding TEM projection. Inset is the SAED pattern along $[30\bar{3}1]$. (C) HRTEM at the tip region, marked in (B), showing facets $\{10\bar{1}3\}$ sharp connected by a small portion of facet (0001). (D) Facet $\{10\bar{1}3\}$, marked in (B), showing the rough surface. Islands with a few atomic layer thickness covered almost the entire surface. (E) Corner between facet $\{10\bar{1}3\}$ and $\{10\bar{1}0\}$, marked in (B), showing multi-atomic-layer steps, induced by the surface energy minimization.

High resolution TEM (HRTEM) images were obtained from the NW tip (shown in Figure 7A) to reveal the lattice structure around the tip edges. The selected NW had a tip predominately covered by the $\{10\bar{1}3\}$ facets (Figure 7B). In general, the NW exhibited a perfect crystal lattice without any observable dislocations. No hint of screw dislocation could be identified. From the very center area, as shown in Figure 7C, a small portion (~ 3 nm) of the (0001) facet could still be observed. It quickly turned into the $\{10\bar{1}3\}$ facets with sharp corners. The lattice spacing of the $\{10\bar{1}3\}$ plane was measured to be 0.1425 nm, consistent with 0.1477 nm calculated from the JCPDS card (No. 36-1451). The $\{10\bar{1}3\}$ facets were found to be rough, as shown in Figure 7D. Islands with a few atomic layer thickness and multiple atomic steps covered almost the entire surface. This could be a result of the surface energy minimization of the crystal system. For the same reason, the $\{10\bar{1}3\}$ facet restructured into a series of multi-atomic-layer steps at the junction with the $\{10\bar{1}0\}$ facet. The rough surface and corners might be responsible for the crystal facet evolution during the NW growth at different temperature and supersaturation, i.e. different driving force of atom diffusion.

Above crystal lattice analysis suggested that the NWs were likely grown by a layer-by-layer mechanism, as we discovered previously. In this mechanism, the Ehrlich–Schwoebel (ES) barrier is a critical parameter that prevents the adatoms from diffusing over the atomic steps and thus builds up necessary adatom concentration to nucleate new atomic layers. In an ideal ZnO NW growth process, atomic layers of the (0001) plane nucleate at the NW tip and grow laterally covering the entire tip surface. Nevertheless, as the (0001) plane approaches the edge, e.g. the

corner with the $(10\bar{1}0)$ plane, new high-index crystal facets will form, such as the $\{10\bar{1}3\}$ and $\{11\bar{2}2\}$ families (Figure 8A). These facets have high surface energy and typically vanish rapidly as their sizes become appreciable (e.g. a few nm wide). Thus, these high-index planes can be considered as metastable intermedia stages as the complete evolvement of a new (0001) plane. However, our observation of the co-existence of these high-index facets within a narrow deposition window suggested that under certain circumstances, these intermedia stages might stably present. For example, the ES barrier for adatoms to diffuse from the (0001) plane to the $(10\bar{1}3)$ plane might be significantly higher than that for adatoms to diffuse backward. Therefore, the overall energy barrier for the formation of a complete new (0001) plane would be much higher than that for leaving the high-energy $(10\bar{1}3)$ plane exposed. Similar scenario would also apply to the facets transition between the pairs of $(0001)/\{11\bar{2}2\}$ and $\{10\bar{1}3\}/\{11\bar{2}2\}$ as we observed experimentally.

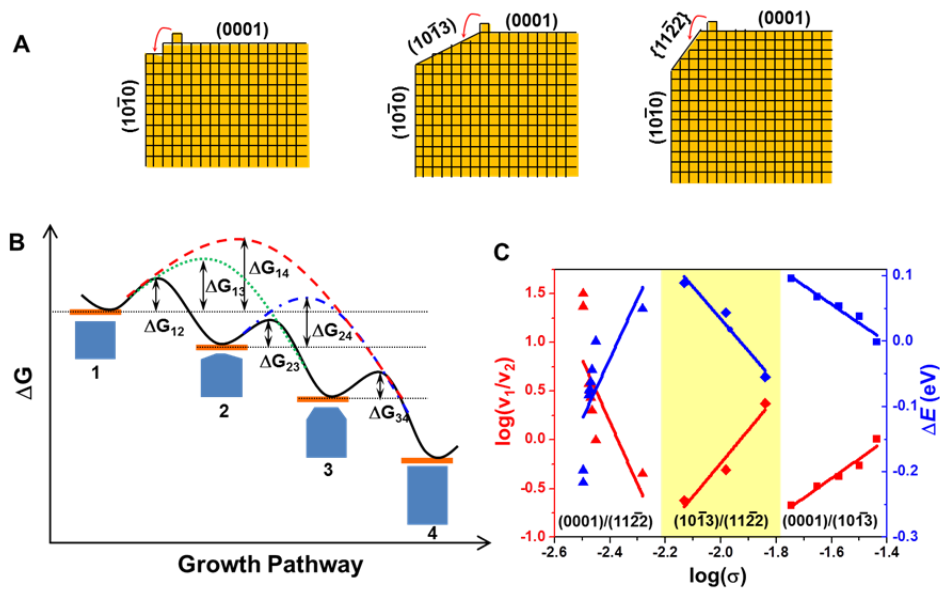


Figure 8. Analogy of facet evolution to the Ostwald-Lussac Law. (A) Schematic of the facet formation model. (B) Schematic energy landscape of a series of facets illustrating the facets evolution pathway. At certain supersaturation, the high-index facets tend to be stable due to the lower energy barriers. (C) Dependence of the growth rate ratio (Left y-axis) and the energy barrier differences (Right y-axis) of $(0001)/\{10\bar{1}3\}$, $\{10\bar{1}3\}/\{11\bar{2}2\}$ and $(0001)/\{11\bar{2}2\}$ on the supersaturation.

This free energy barrier-induced appearance of metastable intermediate stages shares much similarity with the Ostwald-Lussac (OL) Law that has been primarily discovered in biomineralization. The OL law is an empirical law of phase transformation stating that an unstable system does not necessarily transform directly into the most stable phase, but likely into one with the minimum energy loss. Here, we propose that the crystal facet formation could also be represented by a similar energy landscape of the OL law, although the atomic plane growth is not really a phase transformation. In analogy to the OL law, a free energy landscape was constructed to show the ZnO NW tip facets evolution relationships based on our experimental observations.

As shown in Figure 8B, stage 1 to stage 4 represent the process of a complete (0001) atomic layer formation. Stage 4 has the lowest free energy, because of the lowest surface energy of the (0001) plane. In between stages 1 and 4, another two intermediate stages exist, e.g. formation of the $\{10\bar{1}3\}$ facets (stage 2) and formation of the $\{11\bar{2}2\}$ facets (stage 3). These stages have high energy than the final stage 4 because of the higher surface energy of the high-index facets. Kinetically, the corresponding energy barriers between each stage were marked as ΔG_{ab} , where a, b represent the initial and final stage, respectively during the crystal facet growth. As discussed previously, these energy barrier heights might change toward different directions as the ES barrier varies as a function of supersaturation. Under certain circumstances, the energy barriers involving intermediate stages might be significantly lower than ΔG_{14} , and thereby the high-index facets appear in the final NW morphology. The relative value between different ΔG dictates the appearing crystal facet(s). To more specifically elaborate this empirical law of facet evolution, all the experimentally observed NW tip morphology was correlated to ΔG relationships and summarized in Table 1. This table could be further enriched if more new NW tip facets are discovered.

Similar to the OL law for phase transformation, our proposed law for facet evolution at the NW growth front is purely qualitative. Quantification of all the relative energy barriers requires a comprehensive knowledge of various associated energies (e.g. the ES barrier, adsorption/desorption energy, surface energy, etc.) and other parameters (e.g. supersaturation, vibration frequency, etc.), which are beyond the capacity of this work. Fortunately, the facet areas demonstrated a good relation with the supersaturation. According to kinetic Wulff's theorem, the relative growth rates of the facets can be deduced from the relative sizes of them. As discussed earlier, the supersaturation (σ) was considered as the dominating variable in correlation to the deposition location within this small window. Therefore, based on the evolved sizes of the (0001), $\{10\bar{1}3\}$ and $\{11\bar{2}2\}$ facets measured at different deposition locations, the relative growth rate was calculated and plotted as a function of σ (given by the left y-axis in Figure 8C). As the supersaturation decreased, the relative growth rate ratio of (0001)/ $\{10\bar{1}3\}$ decreased from 1.02 to 0.21, and then the relative growth rate ratio of $\{10\bar{1}3\}$ / $\{11\bar{2}2\}$ decreased from 2.38 to 0.24, and finally the relative growth rate ratio of (0001)/ $\{11\bar{2}2\}$ increased from 0.45 to 31.92. The relative growth rate ratio changes indicated that the growth energy barrier difference between the corresponding two groups of facets changed at different supersaturation.

According to the crystal growth theory, the facet growth is linearly related to the supersaturation, and exponentially related to the temperature and the growth energy barrier of corresponding facets, which can be expressed by the equation:

$$v_1 = A\sigma \exp\left(-\frac{E_1}{kT}\right) \quad (1)$$

where v_1 is the growth rate of facet 1, A is a parameter related to the growth condition, E_1 is the growth energy barrier of the facet 1, k is Boltzmann constant and T is the deposition temperature. Using this equation, the energy barrier differences were quantified as a function of σ (given by the right y-axis of Figure 8C). For all of these three pairs of facets, the energy barrier difference might be fitted linearly to the logarithm of the supersaturation, indicating the energy barrier difference was logarithmically influenced by the supersaturation. At higher supersaturation level, corresponding to the location closest to the chamber center, the energy

barrier for the formation of the (0001) facet was almost the same as that of the $\{10\bar{1}3\}$ facets (only 1 meV difference). With the supersaturation decreased, the energy barrier of forming the (0001) facet became much larger than that of the $\{10\bar{1}3\}$ facets, confirming the rapid evolution of the $\{10\bar{1}3\}$ facets in place of the (0001) facet. Similarly, when the supersaturation continued to decrease, the energy barrier for facets $\{10\bar{1}3\}$ changed from being 50 meV smaller than that of the $\{11\bar{2}2\}$ facets to being 90 meV larger than that of the $\{11\bar{2}2\}$ facets, providing a smaller energy barrier for the facet evolution from $\{10\bar{1}3\}$ to $\{11\bar{2}2\}$. As the supersaturation decreased further, the energy barrier for (0001) formation rapidly decreased from 50 meV to -210 meV relative to the energy barrier for $\{11\bar{2}2\}$ formation, confirming a relatively larger drive force for the (0001) to quickly cover the entire NW tip, forming a flat tip surface.

List of Publications:

1. J. Shi, Z. Li, A. Kvit, S. Krylyuk, A.V. Davydov, X.D. Wang, "Electron Microscopy Observation of TiO₂ Nanocrystal Evolution in High-Temperature Atomic Layer Deposition", *Nano Lett.*, 13 5727-5734 (2013).
2. F. Wang, J.-H. Seo, Z. Li, A.V. Kvit, Z. Ma, X.D. Wang "Cl-Doped ZnO Nanowires with Metallic Conductivity and Their Application for High-Performance Photoelectrochemical Electrodes" *ACS Appl. Mater. Interfaces*, 6, 1288–1293 (2014).
3. Y. Mao, P. Zhao, G. McConohy, H. Yang, Y. Tong, X.D. Wang "Sponge-Like Piezoelectric Polymer Films for Scalable and Integratable Nanogenerators and Self-Powered Electronic Systems" *Adv. Energy. Mater.*, 4, 130624 (2014).
4. Y. Yu, X. Yin, A. Kvit, X.D. Wang "Evolution of Hollow TiO₂ Nanostructures via the Kirkendall Effect Driven by Cation Exchange with Enhanced Photoelectrochemical Performance" *Nano Lett.*, 14, 2528–2535 (2014).
5. X.D. Wang, Z. Li, J. Shi, Y. Yu "One-Dimensional Titanium Dioxide Nanomaterials: Nanowires, Nanorods, and Nanobelts" *Chem. Rev.*, 114, 9346–9384 (2014).
6. F. Wang, X.D. Wang "Mechanisms in the solution growth of freestanding two-dimensional inorganic nanomaterials" *Nanoscale*, 6, 6398-6414 (2014).
7. Y. Yu, J. Li, D. Geng, J. Wang, L. Zhang, T.L. Andrew, M.S. Arnold, X.D. Wang "Development of Lead Iodide Perovskite Solar Cells Using Three-Dimensional Titanium Dioxide Nanowire Architectures" *ACS Nano*, 9, 564–572 (2015).
8. H. Hong, F. Wang, Y. Zhang, S.A. Graves, S.B.Z. Eddine, Y. Yang, C.P. Theuer, R.J. Nickles, X.D. Wang, W. Cai "Red Fluorescent Zinc Oxide Nanoparticle: A Novel Platform for Cancer Targeting" *ACS Appl. Mater. Interfaces*, 7, 3373–3381 (2015).

9. Y. Mao, D. Geng, E. Liang, X.D. Wang “Single-electrode triboelectric nanogenerator for scavenging friction energy from rolling tires” *Nano Energy*, 15, 227-234 (2015).
10. H. Li, Y. Yu, M.B. Starr, Z. Li, X.D. Wang “Piezotronic-Enhanced Photoelectrochemical Reactions in Ni(OH)₂-Decorated ZnO Photoanodes” *J. Phys. Chem. Lett.*, 6, 3410–3416 (2015).
11. W. Yang, Y. Yu, M.B. Starr, X. Yin, Z. Li, A. Kvit, S. Wang, P. Zhao, X.D. Wang “Ferroelectric Polarization-Enhanced Photoelectrochemical Water Splitting in TiO₂–BaTiO₃ Core–Shell Nanowire Photoanodes” *Nano Lett.*, 15, 7574–7580 (2015).
12. X. Yin, J. Shi, X. Niu, H. Huang, X.D. Wang “Wedding Cake Growth Mechanism in One-Dimensional and Two-Dimensional Nanostructure Evolution” *Nano Lett.*, 15, 7766–7772 (2015).
13. F. Wang, J.-H. Seo, G. Luo, M.B. Starr, Z. Li, D. Geng, X. Yin, S. Wang, D.G. Fraser, D. Morgan, Z. Ma, X.D. Wang “Nanometer-Thick Single-Crystalline Nanosheets Grown at the Water-Air Interface” *Nature Communications*, 7, 10444 (2016).
14. X. Yin, D. Geng, X.D. Wang “Inverted Wedding Cake Growth Operated by the Ehrlich-Schwoebel Barrier in Two Dimensional Nanocrystal Evolution” *Angew. Chem. Int. Ed.*, 55, 2217-2221 (2016).
15. X. Yin, X.D. Wang “Kinetics-Driven Crystal-Facets Evolution at the Tip of Nanowires – A New Implementation of the Ostwald-Lussac Law” to be submitted (2016).

1.

1. Report Type

Final Report

Primary Contact E-mail**Contact email if there is a problem with the report.**

xudong.wang@wisc.edu

Primary Contact Phone Number**Contact phone number if there is a problem with the report**

6088902667

Organization / Institution name

University of Wisconsin-Madison

Grant/Contract Title**The full title of the funded effort.**

Evolution of Zinc Oxide Nanostructures from Non-Equilibrium Deposition Conditions

Grant/Contract Number**AFOSR assigned control number. It must begin with "FA9550" or "F49620" or "FA2386".**

FA9550-13-1-0168

Principal Investigator Name**The full name of the principal investigator on the grant or contract.**

Xudong Wang

Program Manager**The AFOSR Program Manager currently assigned to the award**

Dr. Ali Sayir

Reporting Period Start Date

03/27/2013

Reporting Period End Date

03/31/2016

Abstract

This project focuses on to quantitatively understand the time-dependent evolution of Zinc Oxide (ZnO) nanostructures driven by non-equilibrium deposition conditions, and thereby establish an experimentally grounded foundation for designing nanostructures and/or functionalities via kinetic control. Morphology is one essential element that gives rise to extraordinary physical, chemical, and mechanical properties in nanomaterials. Precise morphology control of nanomaterials is a notorious task, which heavily relies on fundamental understanding of the governing atomistic mechanisms and kinetics at the nanoscale. Through vapor-solid deposition under dynamically controlled conditions, we observed three unique 1D and 2D nanocrystal growth behavior, which revealed a series of unique growth kinetics at the nanoscale under conditions far away from equilibrium. First, the wedding cake growth mechanism in the formation of 1D and 2D ZnO nanostructures was observed within a narrow growth window. An interesting 1D to 2D morphology transition was also found during the wedding cake growth, when the adatoms overcome the Ehrlich-Schwoebel (ES) barrier along the edge of the top crystal facet triggered by lowering the supersaturation. Furthermore, an inverted wedding cake growth phenomenon was observed in 2D nanostructure evolution. The atomic steps were nucleated along the edge and propagated toward the center forming a unique basin-shaped crown on the tip of each nanowire. The morphology and temperature relation revealed the ES barrier of ZnO to be 0.88 eV. Based on the layer-by-layer growth

DISTRIBUTION A: Distribution approved for public release.

model, a unique high-energy facet evolution phenomenon at the NW tip was observed at different deposition supersaturation within a narrow vapor deposition window. The facets evolution and exposure of high-energy facets were attributed to the fluctuation of the energy barriers for the formation of different crystal facets during the growth of NW tip. This project substantially enriches our understanding on the fundamental kinetics of nanostructured crystal growth and provides a transformative strategy to achieve rational design and control of nanoscale geometry.

Distribution Statement

This is block 12 on the SF298 form.

Distribution A - Approved for Public Release

Explanation for Distribution Statement

If this is not approved for public release, please provide a short explanation. E.g., contains proprietary information.

SF298 Form

Please attach your [SF298](#) form. A blank SF298 can be found [here](#). Please do not password protect or secure the PDF. The maximum file size for an SF298 is 50MB.

[AFD-070820-035.pdf](#)

Upload the Report Document. File must be a PDF. Please do not password protect or secure the PDF. The maximum file size for the Report Document is 50MB.

[AFOSR-final report.pdf](#)

Upload a Report Document, if any. The maximum file size for the Report Document is 50MB.

Archival Publications (published) during reporting period:

1. J. Shi, Z. Li, A. Kvit, S. Krylyuk, A.V. Davydov, X.D. Wang, "Electron Microscopy Observation of TiO₂ Nanocrystal Evolution in High-Temperature Atomic Layer Deposition", *Nano Lett.*, 13 5727-5734 (2013).
2. F. Wang, J.-H. Seo, Z. Li, A.V. Kvit, Z. Ma, X.D. Wang "Cl-Doped ZnO Nanowires with Metallic Conductivity and Their Application for High-Performance Photoelectrochemical Electrodes" *ACS Appl. Mater. Interfaces*, 6, 1288–1293 (2014).
3. Y. Mao, P. Zhao, G. McConohy, H. Yang, Y. Tong, X.D. Wang "Sponge-Like Piezoelectric Polymer Films for Scalable and Integratable Nanogenerators and Self-Powered Electronic Systems" *Adv. Energy. Mater.*, 4, 130624 (2014).
4. Y. Yu, X. Yin, A. Kvit, X.D. Wang "Evolution of Hollow TiO₂ Nanostructures via the Kirkendall Effect Driven by Cation Exchange with Enhanced Photoelectrochemical Performance" *Nano Lett.*, 14, 2528–2535 (2014).
5. X.D. Wang, Z. Li, J. Shi, Y. Yu "One-Dimensional Titanium Dioxide Nanomaterials: Nanowires, Nanorods, and Nanobelts" *Chem. Rev.*, 114, 9346–9384 (2014).
6. F. Wang, X.D. Wang "Mechanisms in the solution growth of freestanding two-dimensional inorganic nanomaterials" *Nanoscale*, 6, 6398-6414 (2014).
7. Y. Yu, J. Li, D. Geng, J. Wang, L. Zhang, T.L. Andrew, M.S. Arnold, X.D. Wang "Development of Lead Iodide Perovskite Solar Cells Using Three-Dimensional Titanium Dioxide Nanowire Architectures" *ACS Nano*, 9, 564–572 (2015).
8. H. Hong, F. Wang, Y. Zhang, S.A. Graves, S.B.Z. Eddine, Y. Yang, C.P. Theuer, R.J. Nickles, X.D. Wang, W. Cai "Red Fluorescent Zinc Oxide Nanoparticle: A Novel Platform for Cancer Targeting" *ACS Appl. Mater. Interfaces*, 7, 3373–3381 (2015).
9. Y. Mao, D. Geng, E. Liang, X.D. Wang "Single-electrode triboelectric nanogenerator for scavenging friction energy from rolling tires" *Nano Energy*, 15, 227-234 (2015).
10. H. Li, Y. Yu, M.B. Starr, Z. Li, X.D. Wang "Piezotronic-Enhanced Photoelectrochemical Reactions in Ni(OH)₂-Decorated ZnO Photoanodes" *J. Phys. Chem. Lett.*, 6, 3410–3416 (2015).
11. W. Yang, Y. Yu, M.B. Starr, X. Yin, Z. Li, A. Kvit, S. Wang, P. Zhao, X.D. Wang "Ferroelectric Polarization-Enhanced Photoelectrochemical Water Splitting in TiO₂–BaTiO₃ Core–Shell Nanowire Photoanodes" *Nano Lett.*, 15, 7574–7580 (2015).
12. X. Yin, J. Shi, X. Niu, H. Huang, X.D. Wang "Wedding Cake Growth Mechanism in One-Dimensional and Two-Dimensional Nanostructure Evolution" *Nano Lett.*, 15, 7766–7772 (2015).

DISTRIBUTION A: Distribution approved for public release.

13. F. Wang, J.-H. Seo, G. Luo, M.B. Starr, Z. Li, D. Geng, X. Yin, S. Wang, D.G. Fraser, D. Morgan, Z. Ma, X.D. Wang "Nanometer-Thick Single-Crystalline Nanosheets Grown at the Water-Air Interface" Nature Communications, 7, 10444 (2016).
14. X. Yin, D. Geng, X.D. Wang "Inverted Wedding Cake Growth Operated by the Ehrlich-Schwoebel Barrier in Two Dimensional Nanocrystal Evolution" Angew. Chem. Int. Ed., 55, 2217-2221 (2016).

2. New discoveries, inventions, or patent disclosures:

Do you have any discoveries, inventions, or patent disclosures to report for this period?

No

Please describe and include any notable dates

Do you plan to pursue a claim for personal or organizational intellectual property?

Changes in research objectives (if any):

N/A

Change in AFOSR Program Manager, if any:

N/A

Extensions granted or milestones slipped, if any:

N/A

AFOSR LRIR Number

LRIR Title

Reporting Period

Laboratory Task Manager

Program Officer

Research Objectives

Technical Summary

Funding Summary by Cost Category (by FY, \$K)

	Starting FY	FY+1	FY+2
Salary			
Equipment/Facilities			
Supplies			
Total			

Report Document

Report Document - Text Analysis

Report Document - Text Analysis

Appendix Documents

2. Thank You

E-mail user

Jun 28, 2016 16:37:33 Success: Email Sent to: xudong.wang@wisc.edu